Chemical Engineering Journal 523 (2025) 168734

Contents lists available at ScienceDirect

Chemical Engineering Journal

journal homepage: www.elsevier.com/locate/cej

Highly sensitive analysis of binary pharmaceuticals in water samples on graphene oxide-confined Cu-MOF composite

Yu-Jen Shih [a,*], Zhi-Lun Wu [a], Wei-Hsiang Chen [a], Yu-Hsuan Liu [a], Chin-Pao Huang [b]

[a] Institute of Environmental Engineering, National Sun Yat-sen University, Taiwan
[b] Department of Civil and Environmental Engineering, University of Delaware, Newark, DE, 19716, USA

ARTICLE INFO

Keywords:
Metal-organic frameworks
Graphene oxide
Electrochemical oxidation
Derived carbon polyhedrons
Selective detection

ABSTRACT

Pharmaceutical pollution in aquatic systems is emerging as a critical environmental concern. The complexity and diversity of drug compounds in real-world water samples pose significant challenges for on-site monitoring. In this study, an electroanalytical strategy was developed for simultaneous quantification of acetaminophen (ACM) and metformin (MTF) in complex water matrices using a 3D-2D cocatalyst composed of metal-organic framework and graphene oxide (Cu-BTC/GO), and its derivative, Cu-carbon polyhedron embedded in reduced graphene oxide (CuCP@rGO). Redox mechanisms responsible for selective detection were elucidated through operando-Raman spectroscopy and density functional theory calculations. Selective quantification was achieved via electrode potential switching, owing to distinct adsorption models: metal-ligand coordination between Cu sites and MTF, and π-π stacking interactions between the sp^2 carbon domains and ACM. Trace levels of pharmaceuticals, ranging from 0.5 to 300 μg L^{-1}, were analyzed in municipal wastewater effluent, lake water, and river water, with detection limits below 0.2 μg L^{-1} for both pollutants. This Cu-C sensing platform offers a practical alternative for frequent, rapid monitoring of pharmaceutical pollutants, with performance comparable to conventional chromatography.

1. Introduction

Substances such as antibiotics, analgesics, and non-steroidal anti-inflammatory drugs (NSAIDs) are classified as emerging pharmaceutical contaminants due to their persistent, bio-accumulative, and ecological risks [1]. These pharmaceuticals frequently occur as multi-component mixture in hospital and municipal wastewaters. Notably, the recent COVID-19 pandemic has led to a significant increase in concentrations, ranging from ng L^{-1} to mg L^{-1} that pose substantial threats to aquatic environment [2]. Many active pharmaceutical ingredients (APIs) resist to degradation and complete mineralization in conventional wastewater treatment plants (WWTPs), often resulting in the formation of toxic disinfection byproducts [3]. Therefore, rapid and accurate monitoring of the distribution of clinical or preclinical drugs in surface water and wastewater is urgently required to mitigate their adverse effects on ecological health. Gas chromatography (GC) and high-performance liquid chromatography (HPLC) are the primary laboratory-scale tools for analyzing trace-level organic pollutants [4]. However, high cost, long turnaround time, lack of portability, and complex sample preparation limit their routine field monitoring applications. In contrast, recent advancements in electrochemical techniques have led to the development of miniature sensors for quantifying both organic and inorganic contaminants [5–7]. The specific electrocatalyst that induces concentration-dependent redox current or resistance response plays a vital role in the electrochemical determination [5,8].

Acetaminophen (ACM), also known as paracetamol, is one of the most prescribed medications for pain relief and fever reduction, and is associated with minimal side effects at therapeutic doses [9]. On the other hand, metformin (MTF) is a biguanide anti-hyperglycemic agent for the treatment of type-II diabetes, and recommended for managing hypoglycemia according to WHO [10]. These pharmaceuticals can be excreted in their unmetabolized forms after consumption; hence, ACM and MTF, which are of the most consumable drugs worldwide [11], are selected in this study to investigate the feasibility of binary-component detection. Owing to the specific reduction potentials of various contaminants, electrochemical methods offer selective quantification, with the merits of short response time and operational simplicity. Carbon materials have emerged as versatile substrates for pharmaceutical sensing, encompassing 0D quantum dots, 1D nanotubes or nanofibers, 2D graphene, and 3D metal organic frameworks (MOFs) or their derived

* Corresponding author.
E-mail address: yjshih@mail.nsysu.edu.tw (Y.-J. Shih).

https://doi.org/10.1016/j.cej.2025.168734
Received 21 July 2025; Received in revised form 16 September 2025; Accepted 19 September 2025
Available online 21 September 2025

carbon architectures [12–14]. Among them, MOFs distribute metal ion nodes within organic linkers with Å-scale homogeneity, such as imidazolate (ZIF), benzene-1,3,5-tricarboxylates (BTC), and benzene-1,4-dicarboxylic acid (BDC) [15]. Transition metals or their oxides in forms of single atoms or nanometer-sized particles can be therefore integrated into a porous, N-enriched carbon matrix upon carbonization under a reduced atmosphere. This architecture significantly enhances the electrochemical surface area (ECSA) and redox sensitivity toward target analytes [16,17].

Our preliminary studies revealed that the sensing currents of MTF were specifically induced by a Cu(I)-to-Cu(II) redox transition under anodic potentials, with optimal sensitivity achieved by decorating Cu NPs on reduced graphene oxide (rGO) [18]. In contrast, the quantification of trace ACM concentrations was strongly governed by the electrode's ECSA, which was greatly enhanced through integration of MOF into the GO structure [19]. Consequently, selective detection was realized by exploiting the distinct oxidation potentials of MTF and ACM. The surface and edge oxygen groups on the sp^2-hybridized carbon domains of GO served as nucleation sites for MOF crystallization [20,21]. In this context, the incorporation of Cu-based MOFs into GO interlayers generated diverse Cu and carbon-active sites, enabling responsive detection of binary pharmaceutical contaminants in wastewater. The novelty of this research lies in the development of a mesoporous carbon sensor derived from pyrolyzing a Cu-BTC/GO precursor, achieving simultaneous quantification of ACM and MTF in mixed solutions. Upon carbonization in a N_2 atmosphere, the MOF-GO architecture transforms into Cu nanoparticles (NPs) encapsulated within carbon polyhedra – mostly octahedrons – dispersed across reduced graphene oxide thin films, forming CuCP@rGO composite. Key parameters, such as the GO-to-Cu ratio and pyrolysis, were optimized to enhance sensor performance in terms of sensitivity, selectivity, analytical recovery, and limit of detection (LOD). To validate the practical applicability of the developed electrodes, calibration for the pharmaceutical pollutants was established in various real-world water samples. The electrochemical mechanisms underlying the sensing current densities of ACM and MTF during anodization were elucidated through voltammetric analysis and free energy calculations.

2. Methods

Supporting Information S1 provides detailed descriptions of the materials and methods, including chemicals, electrode synthesis, characterization, and sensing protocols. The fabrication of Cu-BTC_{1-x}/GO_x and its derived $CuCP_{1-x}$@rGO_x electrodes is depicted in Scheme 1. Briefly, a precursor solution containing $Cu(NO_3)_2{\cdot}3H_2O$ (Fisher Chem., USA), polyvinylpyrrolidone (Sigma Aldrich, USA), and a GO suspension with a defined GO-to-Cu weight ratio (x) was prepared in a solvent of dimethylformamide (DUKSAN, South Korea) and ethanol (J.T.Baker, USA). Benzene-1,3,5-tricarboxylic acid (H_3BTC, Fisher Chem., USA) was then introduced at a Cu-to-BTC ratio of 1:1 to form Cu-BTC/GO via solvothermal synthesis. Finally, CuCP@rGO was obtained by pyrolyzing the Cu-BTC/GO precursor under a N_2 atmosphere.

3. Results and discussion

3.1. Characterization

The morphology of Cu-BTC/GO precursor displays the distribution of BTC frameworks across the GO surfaces, as illustrated in Fig. 1a. This architecture results from the initial adsorption of Cu^{2+} ions onto the oxygenated groups of GO during the solvothermal reaction, followed by coordination with BTC linkers. The Cu-BTC is thus on-site embedded within the graphene plane [22]. Upon pyrolysis at 400 °C, the organic framework undergoes moderate shrinkage (Fig. 1b), forming Cu carbon polyhedrons (CuCP). These 3D CuCP, averaging 200 nm in size, are interconnected to the interlayers of 2D reduced graphene oxide (rGO) wrinkles and folds. The EDS analysis indicates that Cu crystallites anchored around CuCP progressively grow with increasing pyrolysis temperature to 700 °C (Fig. 1c). At higher magnification, the crystallites appear as clusters of Cu nanoparticles, with individual sizes around 10 nm, as revealed in Fig. 1d. Fig. 1e and f illustrates TEM images of Cu-BTC/GO and CuCP@rGO, respectively, highlighting the intercalation of Cu-BTC and CuCP structures within the laminar graphene thin films. After pyrolysis, Cu^{2+} nodes heterogeneously crystalize both on carbon polyhedrons and rGO surfaces. The HRTEM in Fig. 1g evidences the coexistence of metallic Cu and Cu_2O by the selected-area electron diffraction (SAED) recorded in the inset, with lattice fringes exhibiting d-spacing of 0.208 nm and 0.247 nm, respectively [23]. Furthermore, single Cu atoms are also discernible on graphene planes, as shown in Fig. 1h. Elemental mapping of Cu-BTC/GO (Fig. 1i) presents the spatial distribution of C, N, and O signals within the BTC/GO framework, with Cu uniformly dispersed around the BTC polyhedrons. After pyrolysis, CuCP@rGO(400) (Fig. 1j) exhibits long-range ordered copper-carbon crystallinity, where C and N assemble the porous carbon skeleton, and O is concentrated around Cu, suggesting partial oxidation of the copper phase. These mapping results confirm that while the oxygen in GO is largely removed to form rGO, it simultaneously acts as a source for Cu recrystallization into Cu oxides, even under an oxygen-free N_2

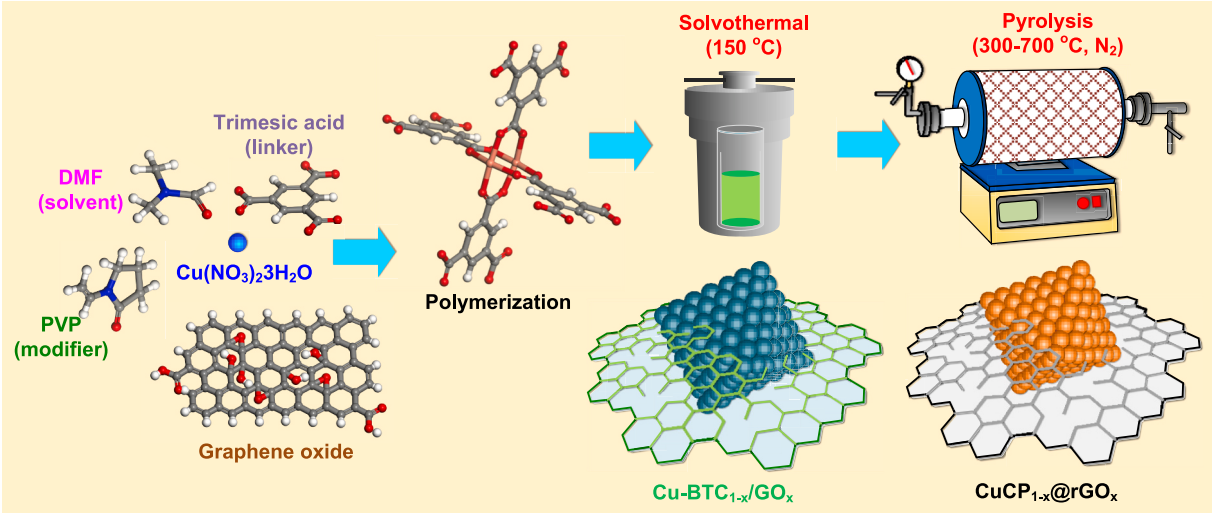

Scheme 1. Procedure of Cu-BTC/GO and the derived CuCP@rGO

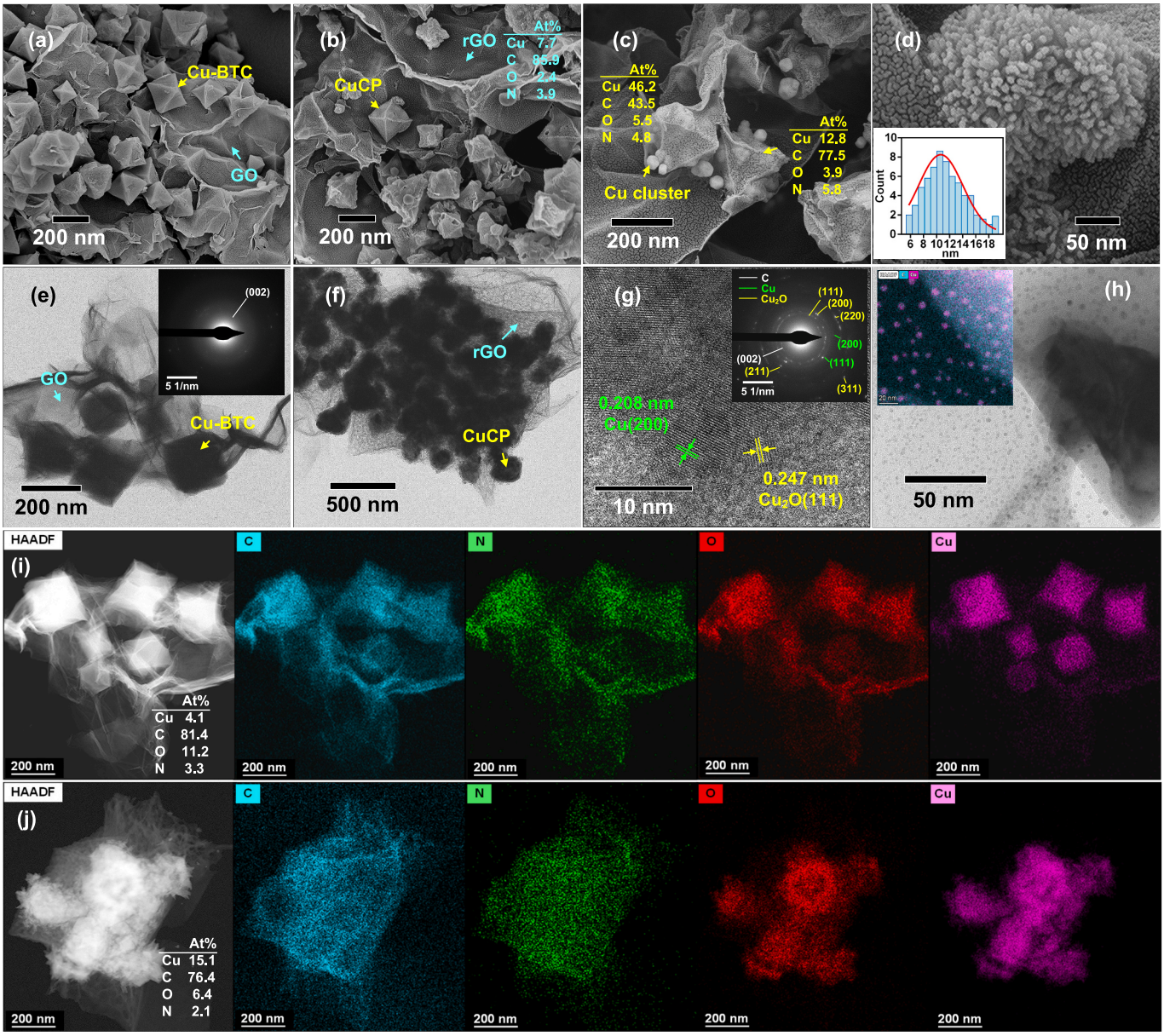

Fig. 1. SEM images of (a) Cu-BTC/GO, CuCP@rGO pyrolyzed at (b) 400 °C and (c) 700 °C, with Cu nanoclusters anchored onto carbon framework. TEM images of (e) Cu-BTC/GO and (f) CuCP@rGO, with selected area electron diffraction (SAED) analysis. (h) Cu NPs decorated onto graphene thin film of CuCP@rGO. TEM elemental mappings of (i) Cu-BTC/GO, and (j) CuCP@rGO(400).

atmosphere.

As shown in Fig. 2a, the XRD pattern of pristine GO reveals a characteristic peak at $2\theta = 12°$, corresponding to the (200) plane with a d-spacing of 7.37 Å. The well-defined diffraction peak of GO reflects the ordered stacking of graphene oxide layers, as further supported by SEM in Fig. S1a. After pyrolysis, the (002) peak broadens and shifts to $2\theta = 24.5°$, corresponding to a reduced interlayer spacing of 3.52 Å. This shift indicates the thermal removal of oxygenated groups and the restoration into less-ordered rGO [24], consistent with the thinner films observed in SEM (Fig. S1b), which resulted from the exfoliation of GO sheets. In Cu-BTC/GO composite, the GO single becomes negligible, while diffraction peaks at 2θ of 6.9°, 9.4°, 11.5°, 13.6°, and 19.1° are assigned to (2 0 0), (2 2 0), (2 2 2), (4 0 0), and (4 4 0) planes, respectively, of the standard HKUST-1 (Cambridge Structural Database 112954) [25]. After heating to 400 °C under a N_2 atmosphere, the BTC peaks vanish. Concurrently, the mixed patterns of metallic copper ($Fm\bar{3}m(225)$) and Cu_2O ($Pn\bar{3}m$, space group 224) emerges [26]. This structural evolution aligns with TEM and elemental mappings, supporting that the decomposition of organic linkers facilitates the in-situ recrystallization of Cu^{2+} ions within CuCP@rGO.

The thermal transformation of Cu-BTC/GO crystal structure is investigated via thermogravimetry, as shown in Fig. 2b. An initial mass loss found around 200 °C is attributed to desorption of bound waters. A subsequent 20 % weight loss, peaking near 300 °C in differential thermal analysis peaking, is associated with the breakdown of the crystal integrity of trimesic acid ligands [27]. Complete carbonization of Cu-BTC/GO into CuCP@rGO structure occurs above 400 °C due to the final mass loss stage. This thermal behavior reflects the simultaneous reduction of Cu^{2+} to Cu and BTC deoxygenation observed in the XRD analysis. The FTIR spectrum of the rGO phase in Fig. 2c displays two prominent vibrational bands for C—O stretching (1400 cm^{-1}) and C═C bonding in conjugated π systems (1565 cm^{-1}), confirming the reduction of graphene structure. In the Cu-BTC/GO composite, additional vibrational features appear in the 600–1700 cm^{-1} range, including the C—N

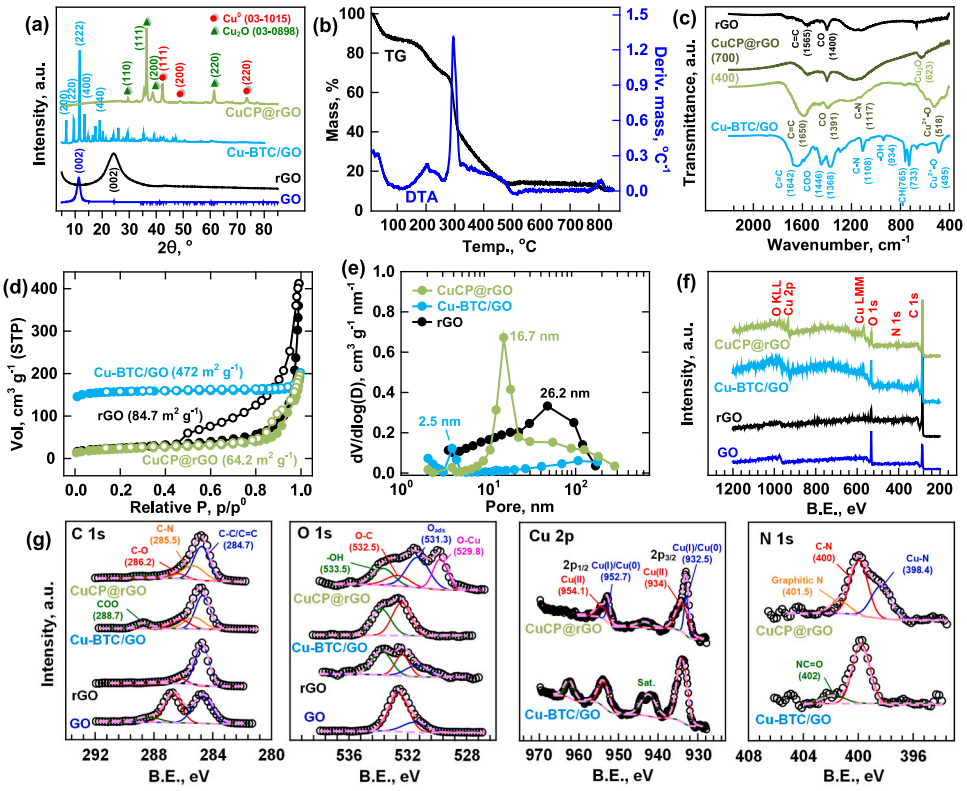

Fig. 2. (a) XRD patterns. (b) Thermal analysis of Cu-BTC/GO. (c) FTIR, (d) BET isotherms, (e) pore size distribution, and (f) full XPS spectra of Cu-BTC/GO, GO, rGO and the derived CuCP@rGO materials, with chemical states deconvoluted at (g) C 1s, O1s, Cu 2p, and N 1s orbitals.

stretching of the PVP additive at 1108 cm^{-1} and the in-plane bending of the benzene ring at 1642 cm^{-1}, indicative of the presence of BTC ligands [28]. After pyrolysis, the carbonyl and carboxyl signals observed at 1446 and 1368 cm^{-1} diminish in CuCP@rGO, consistent with thermal decomposition and reduction of organic components. Furthermore, the Cu-O mode at 495 cm^{-1} represents Cu^{2+} nodes in the MOF. This characteristic vibration shifts to 623 cm^{-1} in CuCP@rGO samples, suggesting the formation of the Cu_2O lattice [29]. Interestingly, although ~5 % residual oxygen and C-O functionalities were identified in a simple rGO sample by EDS (Fig. S1) and FTIR, the oxygen signal appears nearly absent in the rGO regions of the TEM mapping (Fig. 1j). This observation suggests that during thermal reduction, the remaining oxygen species were largely redistributed into copper oxides due to the interaction with Cu^{2+} ions from the Cu-BTC precursor [30].

The specific surface area (S.S.A.) of Cu-BTC/GO precursor reaches 472 $m^2\ g^{-1}$, as determined by the N_2 adsorption isotherm shown in Fig. 2d. The microporosity primarily contributes to this high S.S.A. according to the absence of a hysteresis loop. The significant decline in the S.S.A. to 64 $m^2\ g^{-1}$ for CuCP@rGO treated at 400 °C indicates the narrowing of the micro-interspace within 3D framework, while the emergence of hysteresis in the isotherm confirms the development of mesopores. Notably, a pronounced H2-type loop (defined by the International Union of Pure and Applied Chemistry (IUPAC)) found on rGO sample corresponds to ink-bottle-shaped channels. The mesopore evolution in the CuCP@rGO composite is therefore ascribed to the 2D-3D crosslinking constructed by rGO. The pore size distribution in Fig. 2e reveals the dominant pore sizes, with peaks observed at 2.5 nm, 16.7 nm, and 26.2 nm for Cu-BTC/GO, CuCP@rGO, and rGO, respectively. The increase in mesoporosity after carbonization treatment is anticipated to enhance mass transport and catalytic activity toward the targeted pharmaceutical analytes.

The chemical states of C 1s, O 1s, Cu 2p, and N 1s in the Cu-BTC/GO and the derived CuCP@rGO were examined using XPS spectra, with binding energies centered at around 284 eV, 533 eV, 935 eV, and 400 eV, respectively, as shown in Fig. 2f [31]. The notable declines in O and N signals after pyrolysis reflect their volatilization, while the MOF compound is converted into the composite predominantly composed of Cu and C. Detailed deconvolutions are compiled in Fig. 2g. In C 1s orbital of CuCP@rGO, a significant decrease of the C—O at 287 eV and carboxyl (COO) at 289 eV demonstrates the reduction and carbonization of GO and BTC ligands [32]. Meanwhile, the signal corresponding sp^2-hybridized C═C/C—C at 285 eV becomes dominant, due to the formation of graphitic carbon domains. The remaining C—N bonding at 285.5 eV confirms the incorporation of nitrogen from the PVP additive into the BTC matrix, serving as a dopant in the derived carbon. The O 1s region exhibits an increased relative intensity of adsorbed oxygen (O_{ads}, 531 eV) compared to O—C bond (532.5 eV) in the carbonized framework, in which GO reduced to rGO and Cu^{2+} transition to a Cu_2O phase [33]. The elevated O_{ads} is often associated with the formation of oxygen defect [34]. While high-energy lattice sites with missing O atoms may transiently trap chemical species during their formation and thus evade detection, the persistent O_{ads} signal provides evidence of surface disorder and defect generation within the derived carbon. In the Cu 2p bands, copper ions coordinated as nodes in Cu-BTC primarily exist in the Cu^{2+} state. In CuCP@rGO, the coexisting Cu(II) at 934 eV and Cu(I)/(0) at 932.5 eV [35], with an estimated ratio of 67 % to 33 % evidences the Cu^{2+} reduction to a mixed Cu^0/Cu_2O phase. The original C—N (400 eV) due to the PVP additive is largely replaced with graphitic-N (401.5 eV) and Cu—N bonding (398.4 eV) in N 1 s spectra, indicating N doping into both the carbon matrix and copper species [36]. The thermal-induced chemical transformations collectively profiles the nitrogen-doped carbon frameworks embedded with Cu metal and oxides.

3.2. *Electrochemical properties*

To evaluate the effective surface areas of MOF-derived materials,

voltammetry within a non-Faradaic potential range is carried out (0.1 M phosphate buffer solution (PBS), 10 mV s^{-1}), as shown in Fig. 3a. Both Cu-BTC and Cu-BTC/GO show minimal current responses, whereas the pyrolyzed CuCP@rGO demonstrates greatly enhanced, symmetric capacitive charging/discharging current densities. The electrical double-layer capacitance (EDLC, C_{dl}) is measured using the integrated method [37]:

$$C_{dl}\,(F) = \frac{1}{\nu \Delta V}\int_{V_1}^{V_2}(I_a - I_c)dV \tag{2}$$

where ΔV is the potential window (0.7 V), ν is the scan rate (0.01 V s^{-1}), and I_a and I_c are anodic and cathodic current densities, respectively. rGO alone, used as a control, presents a relatively high electrical capacitance of 43 mF, which contributes majorly to the overall capacitance of CuCP@rGO (116 mF). Additionally, the specific capacitance (C_S) of the glassy carbon substrate (GCE) was independently estimated to be 9.4 mF cm^{-2} (Fig. S2a), using the relation $C_S = \frac{C_{dl,gce}}{A_{gce}}$, where $C_{dl,gce}$ defines the EDLC of GCE and A_{gce} is its geometric area (0.071 cm^2) [38]. The electrochemical surface area (ECSA) of each electrode is then calculated by normalizing EDLC to the GCE reference value obtains ($ECSA = C_{dl}/C_S$) [39]. As shown in Fig. 3b, the ECSA increases from 0.05 cm^2 for Cu-BTC to 0.95 cm^2 for CuCP, while it is greatly boosted with an incorporation of rGO in $CuCP_{1-x}@rGO_x$, reaching a maximum of 12.3 cm^2 at a GO content x = 30 %. For comparison, the ECSA of bare rGO is 4.61 cm^2.

Fig. 3c compares the current-potential response of Cu-BTC/GO and CuCP@rGO electrodes in the presence of binary pharmaceutical pollutants – 1 mM ACM and 1 mM MTF – with rGO serving as a control. A redox couple attributed to reversible oxidation and reduction of ACM (O_{ACM}/R_{ACM}) is observed at +0.5 V and +0.3 V (vs. RHE), respectively, while a distinct oxidation peak for MTF (O_{MTF}) appears at a higher potential of +1.1 V (vs. RHE). These findings indicate that the Cu-carbon composite electrode enables selective detection of coexisting pharmaceuticals through a controlled potential approach. Importantly, the absence of MTF oxidation signals on the rGO electrode (Fig. S2b) underscores the role of site-specific electron transfer in determining selectivity. In other words, ACM is preferentially oxidized at carbon-based sites, while MTF undergoes oxidation at copper-based active sites on CuCP@rGO. The selective detection of ACM and MTF at respective redox potentials in response to varying pollutant concentrations is demonstrated in Fig. 3d. Compared to the voltammetry profiles obtained for each individual pharmaceutical (Fig. S3), the binary solution containing ACM and MTF exhibits negligible impact on the peak potentials of O_{ACM} and O_{MTF}. These two Faradaic reactions are analyzed using the Nicholson and Shain model [40,41]:

$$I_p = 299,000n(ECSA)C_{pham}\left(\alpha D_{pharm}\nu\right)^{1/2} \tag{3a}$$

where D_{pharm} is the diffusion coefficient of ACM ($6.64 \times 10^{-6}\ cm^2\ s^{-1}$) or MTF ($5.6 \times 10^{-6}\ cm^2\ s^{-1}$), C_{pham} is the pollutant concentration ($0.3–1.5 \times 10^{-6}$ mol cm^{-3}), α is the transfer coefficient, obtained from the peak potential E_p and half-peak potential $E_{p/2}$ with,

$$\alpha = \frac{0.0477}{E_P - E_{P/2}} \tag{3b}$$

By calibrating the peak current I_p against concentration, the slope yields the electron number, n, as shown in Fig. 3e. The calculated n value of approximately 2 confirms a nearly two-electron oxidation mechanism for both drugs, provided that the electrochemical surface area (ECSA, Fig. 3b) is measurable. Cyclic voltammetry of CuCP@rGO with varying GO contents (x) in relation to the pollutant concentration is supported in Fig. S3, with the corresponding sensitivities (μA μM^{-1}) reported in Fig. 3f. Since embedding the 3D Cu-BTC framework into 2D GO is essential for increasing ECSA, the GO content must be adjusted to enhance Faradaic current responses. However, excessive incorporation of the carbon-based component restricts the dispersion of Cu nanoparticles within the derived carbon matrix. As a result, the sensitivity toward MTF sharply declines when the GO content exceeds 30 %, while

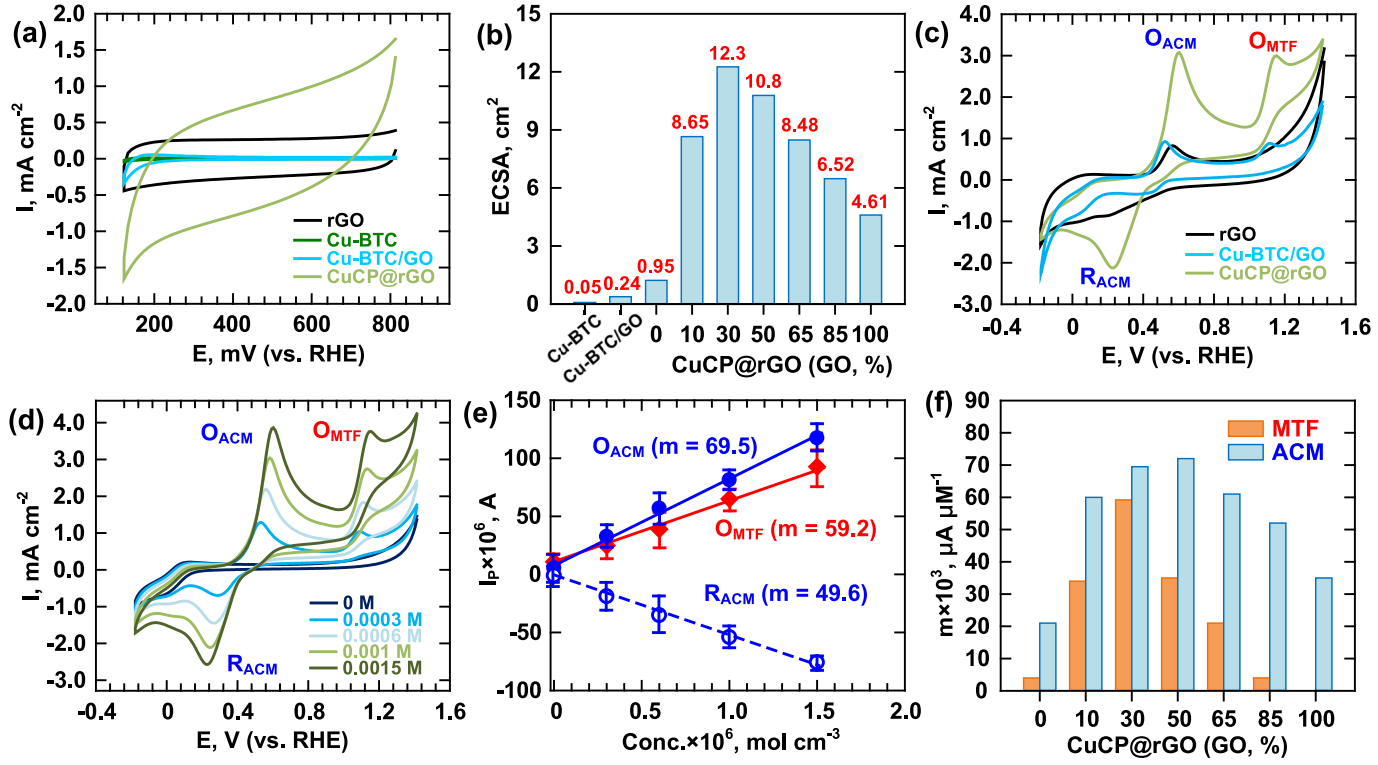

Fig. 3. (a) Voltammetric analysis for capacitive charging process, and corresponding ECSA, as influenced by GO content in the CuCP@rGO composite. (c) Voltammetry in the presence of mixed ACM and MTF (each 1 mM), and (d) effect of pharmaceutical concentration on the redox currents (50 mV s^{-1}, 0.1 M PBS). (e) Linear regression of peak currents for O_{ACM} and O_{MTF} processes versus concentration, (f) with slopes varied with GO content in the CuCP@rGO composite.

the sensitivity for ACM remains relatively unaffected. For practical quantification of binary solution, the composite Cu-$BTC_{0.7}$/$GO_{0.3}$ is selected as the optimal precursor for CuCP@rGO synthesis.

To further elucidate the reaction mechanisms of O_{ACM} and O_{MTF} processes, cycle voltammetry was conducted at varying pH values (0.1 M PBS, 10 mV s^{-1}), as shown in Fig. 4a and b, respectively. Interestingly, the peak current O_{ACM} has a decreasing trend with increasing pH, opposing to O_{MTF}, as displayed in the insets. It is hypothesized that ACM oxidation predominantly occurs at carbon-based sites. The non-polar interactions (i.e., London dispersion forces) between the phenolic group of ACM and the aromatic domains of the CuCP@rGO surface would be weakened upon depronation of the –OH group to $-O^-$ when pH exceeds its acidic constant ($pK_a = 9.4$) [42]. The electrostatic potential (ESP) distribution of ACM molecule with optimized geometry in Fig. 4c indicates increased electron density localized at the O1 atom of phenolic ring after deprotonation, thereby decreasing the Faradaic current density despite anodic polarization. In contrast, MTF possesses two acidic constants for amine $–NH_2^+$ groups, with $pK_{al} = 2.8$ for the H17 atom and $pK_{a2} = 11.5$ for H16 atom [43]. In this scenario, these biguanide moieties become more negatively charged when pH increases, as evidenced by ESP simulation in Fig. 4d. Therefore, the increased electrostatic attraction between the MTF molecule and the Cu-exposed sites enhances the oxidation current under higher pH conditions.

Additionally, the pH-dependent shifts in redox potentials for target pharmaceuticals imply their proton-electron transfer steps. For a generic half-cell reaction, Oxidant + $mH^+ + ne^- \rightleftharpoons$ Reductant; E^0, the Nernst's law describes the dependence of the reduction potential, E, on H^+ concentration:

$$E = E^0 - \frac{RT}{nF} ln\left(\frac{[Re]}{[Ox][H^+]^m}\right) \quad (4a)$$

or at the half-wave potential, $E_{1/2}$, where [Re] = [Ox], and 298 K,

$$E_{1/2} = E^0 - 0.059\frac{m}{n}pH \quad (4b)$$

Here, m and n represent the number of H^+ and e^- in the redox process, respectively [44,45]. As shown in Fig. 4e, the linear regression of the peak potential (E_p) versus pH yields a slope of 52.5 mV per pH for O_{ACM}, while two linear regions are observed for O_{MTF} peak, with slopes of 53.6 mV per pH at pH < 9 and 113 mV per pH at pH > 9. This

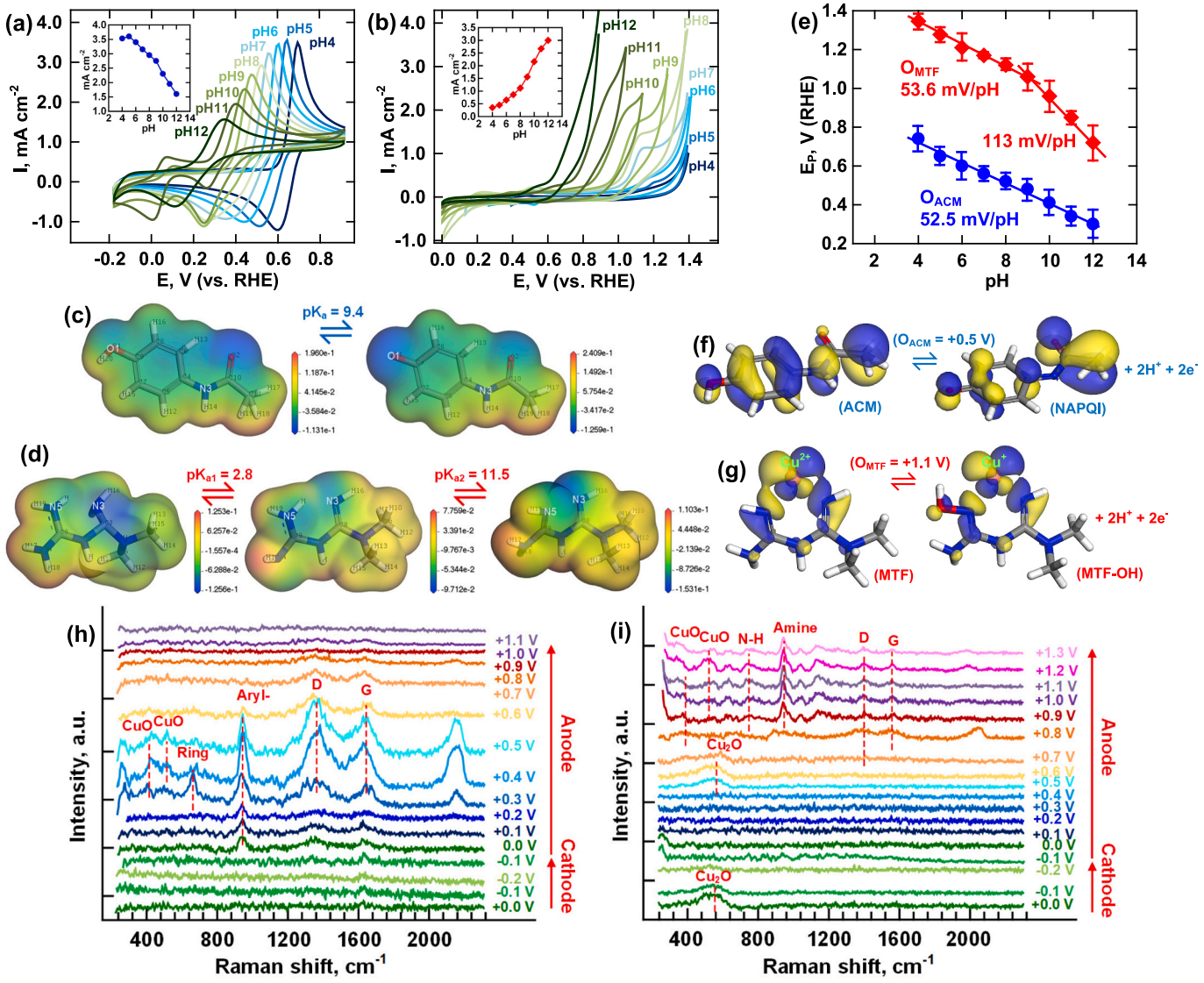

Fig. 4. Effect of pH on voltammetry of CuCP@rGO in 1 mM (a) ACM and (b) MTF, with corresponding linearity of peak potentials O_{ACM} and O_{MTF} against pH. Electrostatic potential distribution of (c) ACM and (d) MTF. HOMO of (f) ACM to NAPQI and (g) MTF to MTF-OH conversions. Operando Raman spectroscopy of CuCP@rGO for (h) ACM and (i) MTF oxidation at varied electrode potentials (vs. RHE).

behavior suggests that both ACM and MTF oxidations involve a $2H^+/2e^-$ mechanism. In addition, an increased proton stoichiometry participates in MTF oxidation at more alkaline conditions. The electron density simulations visualize the highest occupied molecular orbital (HOMO) with electron-rich (blue) and –deficient (yellow) regions. As predicted in Fig. 4f, ACM undergoes oxidative transformation into *N*-acetyl-p-benzoquinone imine (NAPQI) [46], with cleavages of the acetamide N3 and the phenolic hydroxyl O1, resulting in the formation of imine (=N-) and ketone (=O) groups, respectively. On the other hand, the HOMO distribution of MTF coordinated to the Cu site (Fig. 4g) reveals that two amines N3 and N5 are the most susceptible to oxidation. Upon anodization, a metal-ligand charge transfer occurs between Cu(II) and one of the two imino groups in MTF, leading to a two-proton, two-electron redox process to form N-hydroxyguanidine (MTF-OH): $(=NH)_2(Cu(II)) + H_2O \rightarrow (=NH)(-NOH)(Cu(II)) + 2H^+ + 2e^-$ [47]. Additionally, when MTF forms a bidentate complex with the Cu site, additional protons participate in the two-electron oxidation process: $(=NH)_2(Cu(II)) + 2H_2O \rightarrow (-NOH)_2(Cu(0)) + 4H^+ + 2e^-$, at high pH.

Operando Raman spectroscopy was employed to observe the potential-dependent evolution of chemical species on the electrode surface. As shown in Fig. 4h, a signal of aryl-compound (910 cm^{-1}) with amide and hydroxyl ring substituents appears at 0 V, indicating the ACM adsorption [48]. Additional peaks at 450 and 650 cm^{-1} emerge in the potential range of +0.3 V to +0.5 V, which coincides with the onset of O_{ACM} reaction, are attributed to aromatic ring deformation [49]. Two prominent carbon bands at 1320 and 1557 cm^{-1} due to defective sp^3-bonded (D-band) and sp^2 graphitic vibrations (G-band), respectively, are also intensified within this potential window. It is established that non-covalent π-π interactions between phenolic group and carbon texture influence molecular self-assembly, particularly affecting the organization of G-band structures [50]. The subsequent attenuation of these bands at higher potentials implies that the molecular orientation of adsorbed ACM on carbon sites temporarily increases the local crystallinity of carbonaceous framework. In contrast, in the presence of MTF, vibrational bands corresponding to saturated amine at 980 cm^{-1} and N-H wagging at 785 cm^{-1} are observed at potentials beyond +0.9 V, as shown in Fig. 4i, indicating MTF adsorption [51]. This is accompanied by Cu_2O (564 cm^{-1}) transformation into CuO (406 cm^{-1} and 540 cm^{-1}) [52]. A chemical state of Cu_2O-CuO composite in CuCP@rGO electrode persists as MTF accumulates at higher potentials, where the aromatic signals of ACM disappear. These observations confirm that the dual-site Cu-C configuration enables selective detection of ACM and MTF at distinct potentials.

To gain insights into the interactions between drug molecules and the diverse functional surfaces, the free energies of ACM, MTF, and their oxidized intermediates in their adsorbed states are computed, as reported in Fig. 5. The investigated adhesion sites include a Cu-BTC unit, carbon (C), Cu-decorated carbon (Cu/C), and Cu oxides. The corresponding optimized geometries are depicted in Fig. S6 and Fig. S7. Detail DFT methods are provided in the Supporting Information. ACM exhibits strong face-to-face stacking orientation via its phenolic group with the benzene rings in BTC (Fig. 5a), as well as with the aromatic domains in C (Fig. 5b) and Cu/C (Fig. 5c) [53,54], resulting in more negative energies compared to MTF. Interestingly, the MTF molecule adsorbs perpendicularly through Cu-biguanide complexation on Cu sites of Cu-BTC and Cu/C, but reorients into a flatter configuration on C sites

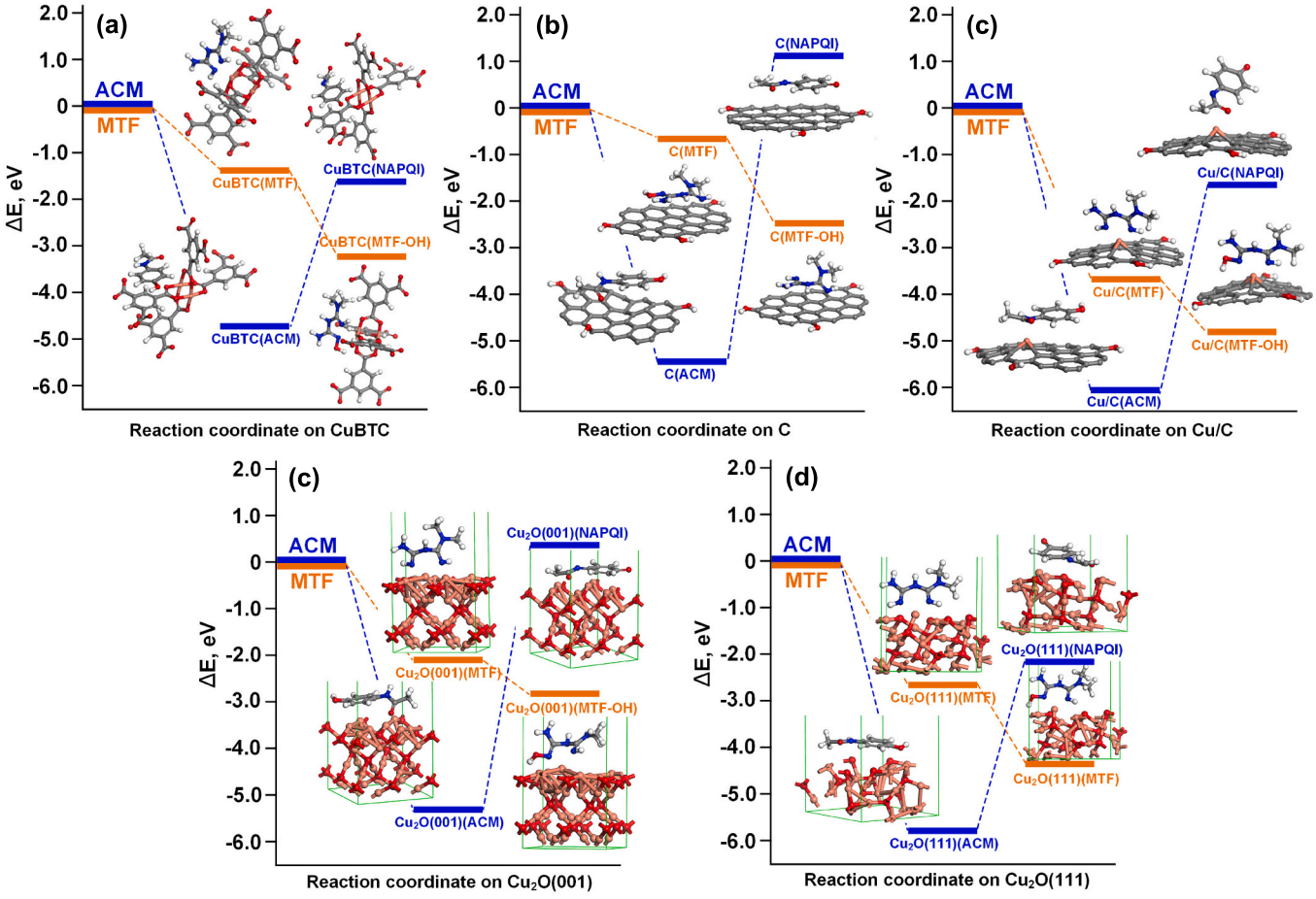

Fig. 5. Free energy evolution for ACM/NAPQI and MTF/MTF-OH conversions on active sites: (a) Cu-BTC, (b) C, (c) Cu/C, and Cu_2O oxide in (d) (0 0 1) and (d) (1 1 1) systems.

with a smaller energy state. These calculations suggest that the non-covalent adsorption of ACM on carbon surfaces – characterized by an average separation distance of around 3.3 Å - is stronger, compared to Cu-biguanide coordination of MTF. Following O_{ACM} step, the resulting NAPQI intermediate undergoes an energetically unfavorable transition, with larger energy barriers. In other words, NAPQI tends to desorb and effectively re-adsorb during the cathode process, thereby supporting the observed reversibility of O_{ACM}/R_{ACM} redox couple in voltammetry. In contrast, when further elevating potential to O_{MTF}, the transformation to N-hydroxyguanidine (MTF-OH) proceeds via a downhill energy pathway. MTF-OH remains perpendicularly connected to the Cu site and is energetically more stable than the adsorbed NAPQI state on C site. On the other hand, adsorbed ACM exhibits a lower energy state on Cu oxide surfaces in both (0 0 1) and (1 1 1) systems than does MTF, through coordination of its acetyl oxygen to Cu sites, as shown in Fig. 5c and d, respectively. However, the oxidation of ACM to NAPQI also results in an uphill transition on these two oxide facets, with energies higher than those of MTF-OH. These DFT simulations suggest that the sensing selectivity between ACM and MTF arises from the differing adsorption energies of their oxidized products. Upon potential switching, the CuCP@rGO surface – where the NAPQI intermediate readily desorbs at low potentials – can expose Cu sites available for subsequent MTF oxidation at higher potentials.

Electrochemical impedances of the derived electrodes during O_{ACM} and O_{MTF} oxidation steps are analyzed as shown in Fig. 6a and b, respectively, with Nyquist plots fitted using the equivalent circuit in the insets [55]. The electronic components include a charge transfer resistance (R_{CT}) in parallel with a double-layer capacitance (C_{dl}), the parallel solid-liquid interfacial resistance (R_L) and capacitance (C_S), and a series electrolyte resistant (R_S), as summarized in Table S1. The R_{CT} values represent the electrode resistance in mediating electrons for the target pharmaceuticals. For ACM at +0.5 V, the trend follows: CuCP@rGO (20.3 Ω) < Cu-BTC/GO (242 Ω) < rGO (245 Ω), and for MTF at +1.1 V, the trend is even more pronounced: CuCP@rGO (28.3 Ω) < Cu-BTC/GO (1872 Ω) < rGO (5481 Ω). These analytical results indicate the essential role of MOF carbonization in enhancing charge transfer efficiency. Notably, the recrystallization of Cu^{2+} nodes into Cu metal of oxide in CuCP@rGO greatly lowers the R_{CT} of O_{MTF} process, compared to pristine MOF and rGO, supporting the preferential adsorption of MTF on Cu sites. Fig. 6c demonstrates the voltammetry over a potential window encompassing both O_{ACM} and O_{MTF} behaviors. The increase in peak currents with varying scan rates characterizes the diffusion-controlled nature of redox processes for both drugs [56]. To diagnose their electrochemical kinetics, a Nernstian model, which predicts a linear shift of the peak potential with $v^{1/2}$, is employed [57,58].

$$E_p = E^{0'} - \frac{RT}{\alpha nF}\left[0.78 + \ln\left(\frac{D_{pharm}^{1/2}}{k^0}\right) + \ln\left(\frac{\alpha nF}{RT}\right)^{1/2} v^{1/2}\right] \quad (5a)$$

Given $\alpha = \frac{0.0477}{|E_p - E_{p/2}|}$, the heterogeneous rate constant (k^0) can be simplified as:

$$k^0 = 2.415\exp\left[-0.02\frac{F}{RT}\right] D_{pharm}^{1/2}\left(E_p - E_{p/2}\right)^{-1/2} v^{1/2} \quad (5b)$$

$$k^0 = 1.11 D_{pharm}^{1/2}\left(E_p - E_{p/2}\right)^{-1/2} v^{1/2} \text{ (at 298 K)} \quad (5c)$$

As shown in Fig. 6c, plots of $\left(E_p - E_{p/2}\right)^{1/2}$ against square-root of scan rate v result in slopes used to calculate the corresponding k^0 values [59]. The CuCP@rGO electrode exhibits k^0 of 0.058 cm s^{-1} for ACM and 0.046 cm s^{-1} for MTF in their respective individual solutions, measured in Fig. S4. When both pharmaceuticals are present in a mixed solution, these values decline to 0.035 cm s^{-1} and 0.037 cm s^{-1} for ACM and MTF, respectively, indicating minimal interference between the two analytes in detection reactivity. The heterogeneous rates for the anodic oxidation of ACM and MTF using $CuCP_{1-x}@rGO_x$ electrodes, as affected by GO content (x, %), are compared in Fig. 6e. Consistent with the Faradaic current responses to pharmaceutical concentrations shown in Fig. 3f, the incorporation of GO contributes to the enhanced ECSA of the 2D-3D composite, which leads to a maximum k^0 for ACM at x = 30–50 %. However, as the GO content increases, the relative abundance of Cu oxide diminishes, resulting in a sharp decline in the k^0 value for MTF at x exceeding 30 %. EPR analysis in Fig. 6f reveals a weaker signal associated with oxygen vacancies (O_V) in the rGO sample, compared to CuCP.

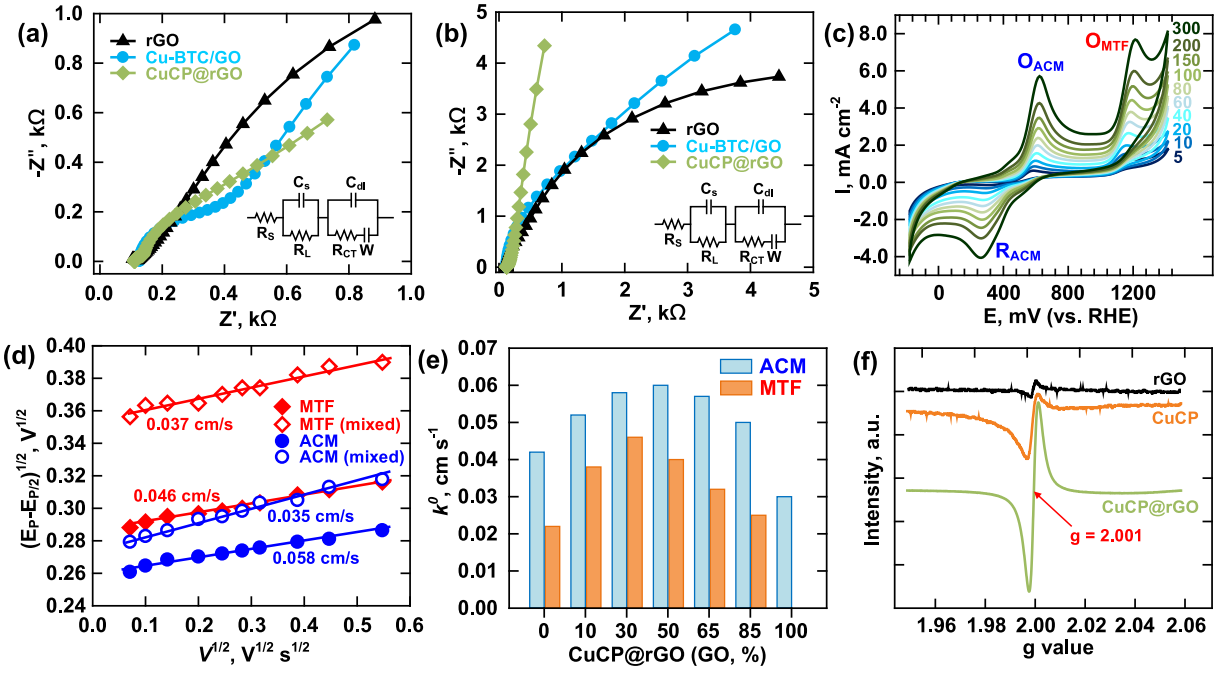

Fig. 6. Impedance analysis at potentials of (a) +0.5 V and (b) +1.1 V in a binary pharmaceutical solution (1 mM ACM, 1 mM MTF, 0.1 M PBS). (c) Effect of scan rate on voltammetry of CuCP@rGO electrode (1 mM ACM + MTF), with (d) linearity of peak profile, $(E_p - E_{p/2})^{1/2}$, against the scan rate $v^{1/2}$. (e) Heterogeneous rate constants of ACM and MTF oxidation as affected by GO content in the CuCP@rGO composite. (f) EPR analysis in the region of oxygen vacancy.

Notably, the CuCP@rGO composite exhibits an identified O_V peak with a g-value of 2.001, corresponding to unpaired electrons trapped at defects [60]. The enriched oxygen defects mainly originate from the mixed-valence state of Cu(0)/Cu(I) formed during carbonization, thereby improving electron mobility for oxidation reactions, as observed in both impedance and heterogeneous rate analyses.

3.3. Electrochemical sensing of binary ACM and MTF

Differential pulse voltammetry (DPV) was employed to quantify trace levels of ACM and MTF in mixed solution, with both analytes ranging in 0.5–300 μg L^{-1} (0.1 M PBS, pH 8). As demonstrated in Fig. 7a, the rGO electrode presents one sharp O_{ACM} peak at +0.5 V, while the O_{MTF} signal is nearly imperceptible – further confirming that ACM detection primarily occurs at carbon sites. In contrast, Fig. 7b and c displays the DPV analysis of the Cu-BTC/GO and CuCP@rGO electrodes, respectively, toward increasing concentrations of binary pharmaceutical mixture. A substantial enhancement in the O_{MTF} peak intensity is observed, indicating the critical role of Cu sites in MOF composites. Notably, the O_{MTF} current becomes even more pronounced with the CuCP@rGO sensor. This result further highlights that the enlarged ECSA and the phase transition of Cu^{2+} to Cu_2O in the carbonized composite significantly improve the MTF sensitivity. Plots of peak current I_P versus pharmaceutical level present two obvious linear regions: 0.5–50 μg L^{-1} (low) and 50–300 μg L^{-1} (high), as shown in Fig. 7d and e for ACM, and Fig. 7f and g for MTF at their respective peak potentials. Generally, the sensitivity in μA per μg L^{-1} is considerably higher in the low concentration range compared to high range. The calibration slopes m for O_{ACM} follow the order: 0.566 μA $μg^{-1}$ L (CuCP@rGO) > 0.144 μA $μg^{-1}$ L (Cu-BTC/GO) > 0.103 μA $μg^{-1}$ L (rGO). In contrast, the slopes for O_{MTF} are in the order: 0.905 μA $μg^{-1}$ L (CuCP@rGO) > 0.204 μA $μg^{-1}$ L (Cu-BTC/GO) > 0.0053 μA $μg^{-1}$ L (rGO). The limit of detection (LOD) and limit of quantification (LOQ) are calculated based on the standard equations: $LOC = \frac{3\sigma}{m}$ and $LOQ = \frac{10\sigma}{m}$. Using the CuCP@rGO electrode, the standard deviation σ of background current is obtained from DPV analysis in the blank solution ($n = 10$, 2.96×10^{-8} A for ACM at +0.5 V, and 6.34×10^{-8} for MTF at +1.1 V). As a result, LOD and LOQ are 0.16 μg L^{-1} and 0.52 μg L^{-1} for ACM, and 0.21 μg L^{-1} and 0.69 μg L^{-1} for MTF, respectively, in mixed pharmaceutical solutions.

The detection of binary pharmaceuticals was evaluated in various real water samples, compositions detailed in Table S2, to validate the applicability of the CuCP@rGO electrode. Based on DPV results shown in Fig. S5, Fig. 7h and i demonstrates the calibration plots for ACM (at +0.5 V) and MTF (at +1.1 V), performed in the effluent from a municipal wastewater treatment plant (WWTP), Chengcing Lake, and the Liver River, all located in Kaohsiung City, Taiwan. Compared to the results obtained in PBS electrolyte, the water matrices have negligible influence on ACM detection, with an average sensitivity of 0.6 μA $μg^{-1}$ L. However, the slopes for MTF noticeably decrease to 0.52, 0.32, and 0.44 μA $μg^{-1}$ L in WWTP, River, and Lake samples. The Faradaic current associated with the O_{MTF} process is more susceptible to the water complexity than the O_{ACM} process. Fig. 7j displays the voltammetry recorded in different water samples over a potential window (v = 50 mV s^{-1}) that includes O_{ACM} and O_{MTF} peaks. The absence of interfering peak currents

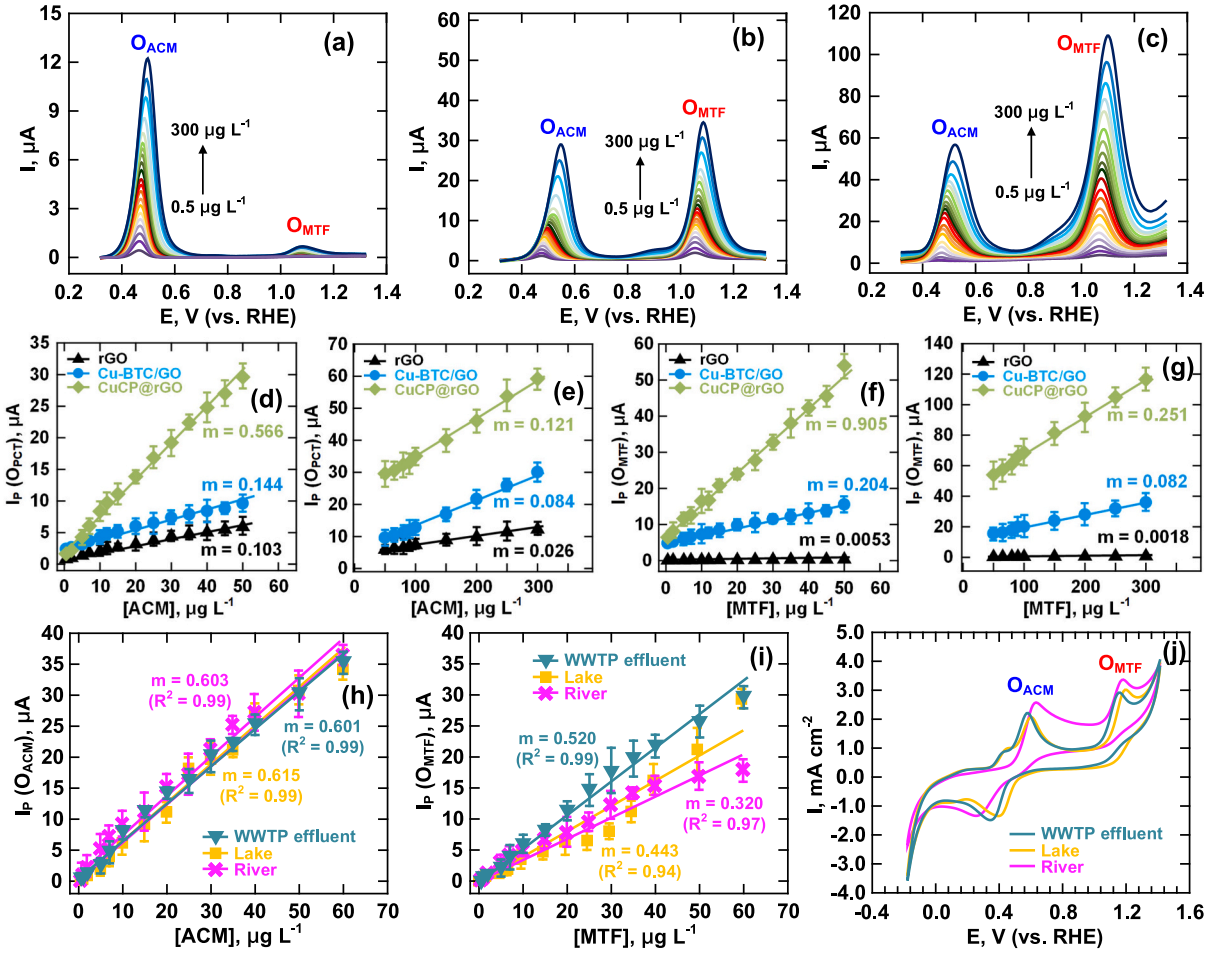

Fig. 7. DPV current responses of (a) rGO, (b) Cu-BTC/GO, and (c) CuCP@rGO electrodes to varied pharmaceutical concentrations in the binary solution. Calibration curves for (d) low and (e) high concentrations of ACM, and (f) low and (g) high concentrations of MTF. Effect of water matrices on sensing (h) ACM and (i) MTF. (j) Voltammetric analysis of CuCP@rGO electrode for 1 mM ACM and MTG spiked in real water samples.

confirms that other components in the matrices have minimal impact on the detection of target drugs. However, the weakened sensitivity to MTF in River sample is likely due to its elevated salinity. As a brackish water body with an ionic strength of 0.7 eq. L^{-1}, it contributes to a higher non-Faradaic capacitive current that obscures the resolution of O_{MTF} peak.

A comprehensive review of active materials for electrochemical quantification of ACM and MTF is reported in Table S3. Various carbon-basd materials – such as CNT [61], graphene [62,63], and MOFs [64], as well as metal oxides, such as $SrWO_4$ [65], Ni [66,67], Cu [68], and Au [69], have been explored as sensing platforms. Incorporating transition metals into different carbonaceous textures generally lowers the detection limits for ACM, clarifying the contribution of carbon to enhancing selectivity [70–73]. Additionally, sensing MTF relies on the formation of Cu(II)-biguanide complexes as a redox mediator for inducing Faradaic currents. Thus, Cu composites are frequently chosen [47,74–76]. However, electrode characteristics optimized for high sensitivity to a single target pollutant often limit versatility when applied to solutions containing multiple contaminates. In the present study, a bi-functional co-catalyst was synthesized using Cu-MOF and GO as precursor, enabling tunable decoration of Cu NPs into 3D carbon framework to boost sensitivity toward binary mixtures of ACM and MTF. Moreover, the sensor demonstrated reliable performance in various real-world water samples.

Repetitive cyclic voltammetry are conducted in a mixed solution containing 0.5 mM ACM and 0.5 mM MTF using the CuCP@rGO electrode to assess its sensor durability. As shown in Fig. 8a, the current responses for O_{ACM} and O_{MTF} stabilize within the first 10 cycles, and remain consistent over the subsequent 100–5000 cycles. Both peak currents possess minimal decay, with standard deviations below 5 %, verifying the excellent electrochemical stability of the electrode for long-term redox process. Fig. 8b presents the DPV responses of 5 μg L^{-1} mixed pharmaceuticals spiked into the WWTP sample over 15 replicated tests. The current signals of the O_{ACM} and O_{MTF} doublet show minimal variation, with mean recoveries $\bar{P}$ of 98.8 ± 2.56 % for ACM and 101.8 ± 6.4 % for MTF. The associated control charts are depicted in Fig. S8, alongside results from HPLC analysis. Although conventional chromatography (Fig. S9) achieves relatively lower detection limits for ACM and MTF, the CuCP@rGO sensor delivers comparable recovery values, which all measurements fall within the defined warning limits ($\bar{P} \pm 2\sigma$) and control limits ($\bar{P} \pm 3\sigma$), validating the quantification accuracy of the sensor for these target pollutants. The selectivity of the CuCP@rGO toward mixed ACM and MTF is further assessed through stepwise addition of interfering chemicals under chronoamperometry mode. As shown in Fig. 8c, the amperometric currents are recorded at respective potentials (+0.5 V and +1.1 V). Following sequential additions of ACM or MTF, the

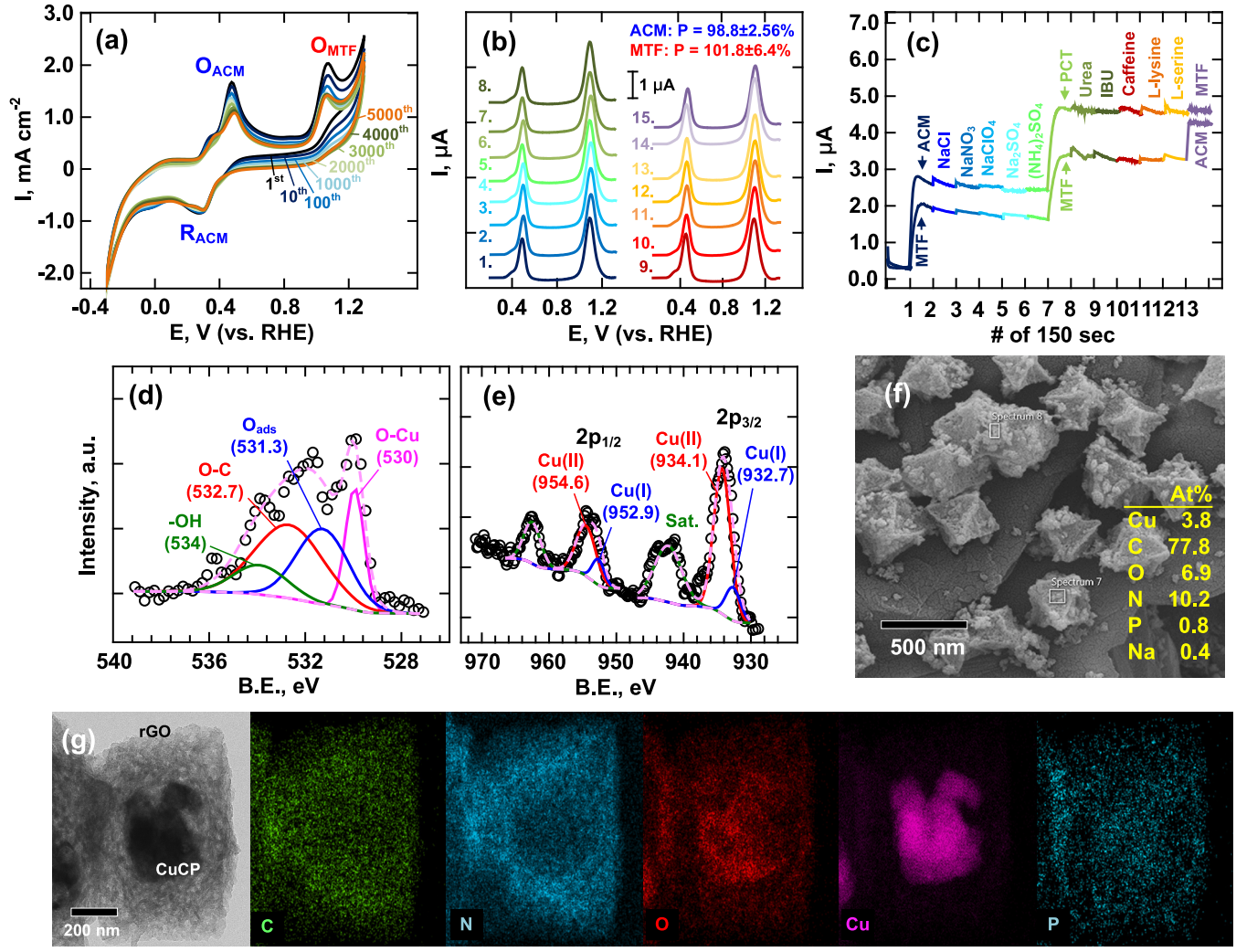

Fig. 8. (a) Repetitive cyclic voltammetry curves of the CuCP@rGO electrode in the presence of 0.5 mM mixed ACM/MTF. (b) Reproducibility test of DPV signals of ACM/MTF (each 5 μg L^{-1}) spiked in WWTP effluent over 15 replicated trails. (c) Effects of interfering species (inorganic salts = 1 mM, organic matters = 5 μg L^{-1}) on chronoamperometric currents of ACM (+0.5 V) and MTF (+1.1 V). XPS analysis of the used electrode at (d) O 1s and (e) Cu 2p orbitals. (f) SEM morphology and (g) TEM mappings of the used CuCP@rGO.

measurement of steady currents lasts for 150 s for each of chemicals, including inorganic salts – NaCl, $NaNO_3$, $NaClO_4$, Na_2SO_4, and $(NH_4)_2SO_4$) and organic compounds – urea, ibuprofen (IBU), caffeine, L-lysine, and L-serine. At anodic potentials, while a brief capacitive charging is observed due to ionic strength perturbation, none of anionic species at 1 mM causes significant shifts in the Faradaic current response of either drugs. Organic matters, frequently found in wastewater, also exhibit minimal interference. Interestingly, the ACM current remains stable in the presence of MTF, whereas the MTF current notably elevates after ACM is introduced. Since the applied potential for O_{MTF} is beyond O_{ACM}, the overlapping transient current from ACM could affect the MTF calibration in mixed solutions. To mitigate this interference during practical operation, applying a range of potentials is advised to pre-screen for the simultaneous presence of ACM and MTF.

The used CuCP@rGO electrode, obtained after repetitive voltammetry tests, was analyzed by XPS, as shown in Fig. 8d and e. Compared to the pristine sensor (Fig. 2g), significant changes are observed in the elemental ratios, particularly in O-C at O 1s and Cu(II) at Cu 2p orbitals, which increase from 16 % and 65 % to 31 % and 83 %, respectively. These post-characterizations indicate partial passivation of Cu and oxidation of functional groups on reduced graphene, attributed to their role in mediating electron transfer for the oxidation of adsorbed pollutants. The shift in chemical states is further supported by an increase in the atomic oxygen content, as displayed in Fig. 8f, while the 3D framework of CuCP octahedrons uniformly anchored on graphene sheets remains intact. Fig. 8g re-examines TEM mappings of the used CuCP@rGO electrode, showing the retained topological structure of CuCP intercalated within rGO phase. Cu and O elements are predominantly localized in polyhedral domains, encapsulated by C and N signals. Additional P element well-distributed around the carbon skeleton is due to the adsorption of phosphate buffer.

4. Conclusions

Pharmaceutical pollution in aquatic environment poses potential risks to both ecological systems and human health. To improve the field-deployable detection of pharmaceuticals in water samples, a convenient and rapid quantification method is highly desirable. In this study, a Cu-C composite, CuCP@rGO, was synthesized from a MOF and graphene oxide to engineer multiple adsorption sites for sensing mixed pharmaceutical compounds, ACM and MTF. Specifically, Cu NPs confined within the carbon octahedral framework served as coordination centers for MTF, whereas π-π interactions between the carbon domains and ACM facilitated reversible redox processes at distinct potentials. The incorporation of GO at an optimal ratio promoted the uniform distribution of Cu sites, thereby boosting electrode sensitivity. Selective detection was fulfilled bypotential switching, +0.5 V (vs. RHE) for ACM and +1.1 V (vs. RHE) for MTF. To validate the sensor applicability, trace concentrations at μg L^{-1} level were successfully quantified in complex water matrices, including municipal wastewater effluent, lake water, and river water. This study offers insights into the design of MOF-GO-based electrochemical sensors and presents a promising platform for pharmaceutical monitoring, achieving detection limits comparable to those obtained using chromatographic methods.

CRediT authorship contribution statement

Yu-Jen Shih: Writing – review & editing, Writing – original draft, Visualization, Validation, Supervision, Software, Resources, Project administration, Investigation, Funding acquisition, Conceptualization. **Zhi-Lun Wu:** Methodology, Investigation, Formal analysis, Data curation. **Wei-Hsiang Chen:** Resources, Methodology, Formal analysis, Data curation. **Yu-Hsuan Liu:** Methodology, Investigation, Formal analysis, Data curation. **Chin-Pao Huang:** Validation, Methodology, Investigation, Conceptualization.

Declaration of competing interest

The authors declare that they have no known competing financial interests or personal relationships that could have appeared to influence the work reported in this paper.

Acknowledgement

The authors would like to thank the National Science and Technology Council, Taiwan for generous finance support of this research project under Contract No. NSTC 111-2223-E-110-003-MY4.

Appendix A. Supplementary data

Supplementary data to this article can be found online at https://doi.org/10.1016/j.cej.2025.168734.

Data availability

Data will be made available on request.

References

[1] D. Lakshmi S, V. Geetha B, V. Murali, From prescription to pollution: the ecological consequences of NSAIDs in aquatic ecosystems, Toxicol. Rep. 13 (2024) 101775, https://doi.org/10.1016/j.toxrep.2024.101775.
[2] S.R. Maremane, G.N. Belle, P.J. Oberholster, E.O. Omotola, Occurrence of selected Covid-19 drugs in surface water resources: a review of their sources, pathways, receptors, fate, ecotoxicity, and possible interactions with heavy metals in aquatic ecosystems, Environ. Geochem. Health 47 (2025) 3, https://doi.org/10.1007/s10653-024-02293-9.
[3] Y.D. Astuti, A. Nastiti, R.D. Larasati, D. Roosmini, M.S. Abfertiawan, Occurrence and removal efficiency of active pharmaceutical ingredients (APIs) in wastewater treatment plants: a systematic review from Southeast Asia, ACS EST Water 4 (2024) 4253–4263, https://doi.org/10.1021/acsestwater.4c00385.
[4] D. Fatta, A. Nikolaou, A. Achilleos, S. Meric, Analytical methods for tracing pharmaceutical residues in water and wastewater, Trends Anal. Chem. 26 (2007) 515–533, https://doi.org/10.1016/j.trac.2007.02.001.
[5] E. Boselli, Z. Wu, A. Friedman, B.C. Henn, I. Papautsky, Validation of electrochemical sensor for determination of manganese in drinking water, Environ. Sci. Technol. 55 (2021) 7501–7509, https://doi.org/10.1021/acs.est.0c05929.
[6] R. Khan, Z.O. Uygun, D. Andreescu, S. Andreescu, Sensitive detection of perfluoroalkyl substances using MXene–AgNP-based electrochemical sensors, ACS Sens. 9 (2024) 3403–3412, https://doi.org/10.1021/acssensors.4c00776.
[7] K. Chen, S. Liu, Y. Zhou, G. Zhao, Monitoring and analysis of total tetracyclines in water from different environmental scenarios using a designed broad-spectrum aptamer, Environ. Sci. Technol. 59 (2025) 5736–5746, https://doi.org/10.1021/acs.est.4c12923.
[8] P. Manimaran, E. Tamilalagan, S.M. Chen, A. Govindharaj, Development of an ultrasensitive sensor for detecting metol in environmental water samples using ruddlesden-popper type layered perovskite (La_2NiO_4) combined with graphene oxide, Water Res. 273 (2025) 122998, https://doi.org/10.1016/j.watres.2024.122998.
[9] S.H. Alrefaee, M.M. Aljohani, I.S.S. Alatawi, A. Almahri, K.S. Alrashdi, S.F. Bin-Ibrahim, H.M. Abumelha, N.M. El-Metwaly, Removal of acetaminophen from wastewater using a novel bimetallic La/Th metal-organic framework: kinetics, thermodynamics, isotherms, and optimization through Box-Behnken design, Proc. Saf. Environ. Prot. 189 (2024) 1134–1150, https://doi.org/10.1016/j.psep.2024.06.046.
[10] U. Lertxundi, S. Domingo-Echaburu, S. Barros, M.M. Santos, T. Neuparth, J. B. Quintana, R. Rodil, R. Montes, G. Orive, Is the environmental risk of metformin underestimated? Environ. Sci. Technol. 57 (2023) 8463–8466, https://doi.org/10.1021/acs.est.3c02468.
[11] M.R. Elamin, B.Y. Abdulkhair, F.K. Algethami, L. Khezami, Linear and nonlinear investigations for the adsorption of paracetamol and metformin from water on acid-treated clay, Sci. Rep. 11 (2021) 13606, https://doi.org/10.1038/s41598-021-93040-y.
[12] S. Taioli, Enabling materials by dimensionality: From 0D to 3D carbon-based nanostructures, in: T. Onishi (Ed.), Theoretical Chemistry for Advanced Nanomaterials, Springer, Singapore, 2020, https://doi.org/10.1007/978-981-15-0006-0_5.
[13] J. Zhu, X.F. Lu, D. Luan, X.W. Lou, Metal–organic frameworks derived carbon-supported metal electrocatalysts for energy-related reduction reactions, Angew. Chem. Int. Ed. 63 (2024) e202408846, https://doi.org/10.1002/anie.202408846.
[14] I. Chajanovsky, S. Cohen, D. Muthukumar, G. Shtenberg, R.Y. Suckeveriene, Enhancement of integrated nano-sensor performance comprised of electrospun PANI/carbonaceous material fibers for phenolic detection in aqueous solutions, Water Res. 246 (2023) 120709, https://doi.org/10.1016/j.watres.2023.120709.

[15] M. Ezzati, S. Shahrokhian, H. Hosseini, In situ two-step preparation of 3D NiCo-BTC MOFs on a glassy carbon electrode and a graphitic screen printed electrode as nonenzymatic glucose-sensing platforms, ACS Sustain. Chem. Eng. 8 (2020) 14340–14352, https://doi.org/10.1021/acssuschemeng.0c03806.
[16] A.H. Sharifabad, S.A. Safavi-Mirmahalleh, M. Golshan, M. Sienkiewicz, M.R. Saeb, M. Salami-Kalajahi, Metal-organic frameworks (MOFs)-based hybrid structures in developing glucose sensors, Chem. Eng. J. 512 (2025) 161513, https://doi.org/10.1016/j.cej.2025.161513.
[17] S. Pathan, J. Raveendran, M. Memon, V. Chavda, K. Niyas, J. Bayry, P. Abdul Rasheed, Upcycling of electronic waste into a Cu-based metal–organic framework: from cell phone to a disposable electrochemical bilirubin sensor, Chem. Eng. J. 511 (2025) 162217, https://doi.org/10.1016/j.cej.2025.162217.
[18] Y.J. Shih, Y.Q. Su, W.H. Chen, S.K. Lin, Y.C. He, C.P. Huang, Copper nanoparticles encapsulated in reduced graphene oxide electrode (Cu_xrGO_{1-x}) for the electrochemical quantification of metformin in water, Chem. Eng. J. 471 (2023) 144676, https://doi.org/10.1016/j.cej.2023.144676.
[19] Y.J. Shih, S.K. Lin, Z.L. Wu, W.H. Chen, Cobalt and zinc imidazolate encapsulated in reduced graphene oxide and the derived nitrogen-enriched carbon frameworks (CoNC@rGO) for electrochemically sensing acetaminophen (APAP), Chem. Eng. J. 481 (2024) 148437, https://doi.org/10.1016/j.cej.2023.148437.
[20] C.O. Ania, M. Seredych, E. Rodriguez-Castellon, T.J. Bandosz, New copper/GO based material as an efficient oxygen reduction catalyst in an alkaline medium: the role of unique Cu/rGO architecture, Appl. Catal. Environ. 163 (2015) 424–435, https://doi.org/10.1016/j.apcatb.2014.08.022.
[21] M.S. More, G.A. Bodkhe, F. Singh, M. Kim, M.D. Shirsat, Metal–organic framework-reduced graphene oxide (Zn-BDC@rGO) composite for selective discrimination among ammonia, carbon monoxide, and sulfur dioxide, Appl. Phys. A 129 (2023) 828, https://doi.org/10.1007/s00339-023-07103-0.
[22] V. Saravanakumar, V. Rajagopal, M. Kathiresan, V. Suryanarayanan, S. Anandan, K.C. Ho, Cu-MOF derived CuO nanoparticle decorated amorphous carbon as an electrochemical platform for the sensing of caffeine in real samples, J. Taiwan Inst. Chem. Eng. 133 (2022) 104248, https://doi.org/10.1016/j.jtice.2022.104248.
[23] N. Gyawali, I. Lee, S. Shrestha, S. Acharya, A.A.S.M. Zahid, K. Kim, K.P. Sapkota, J. R. Hahn, MOF-derived in situ confinement of copper/copper oxide nanoparticles inside a carbon tube: a facile morphologically controlled synthesis strategy for superior visible-light-driven photocatalytic efficiency, Ind. Eng. Chem. Res. 64 (2025) 5212–5227, https://doi.org/10.1021/acs.iecr.4c03977.
[24] B.A. Aragaw, Reduced graphene oxide-intercalated graphene oxide nano-hybrid for enhanced photoelectrochemical water reduction, J. Nanostruct. Chem. 10 (2020) 9–18, https://doi.org/10.1007/s40097-019-00324-x.
[25] D.G. Madden, D. O'Nolan, N. Rampal, R. Babu, C. Çamur, A.N. Al Shakhs, S. Y. Zhang, G.A.R. Perez, N.P.M. Casati, C. Cuadrado-Collados, D. O'Sullivan, N. P. Rice, T. Gennett, P. Parilla, S. Shulda, K.E. Hurst, V. Stavila, M.D. Allendorf, J. Silvestre-Albero, A.C. Forse, N.R. Champness, K.W. Chapman, D. Fairen-Jimenez, Densified HKUST-1 monoliths as a route to high volumetric and gravimetric hydrogen storage capacity, J. Am. Chem. Soc. 144 (2022) 13729–13739, https://doi.org/10.1021/jacs.2c04608.
[26] F. Hasani, J.B. Raoof, M. Ghani, R. Ojani, Nanoporous carbon fiber derived from Cu-BDC metal organic framework @pencil graphite as a sorbent for solid phase microextraction of acetamiprid and imidacloprid, Anal. Chim. Acta 1278 (2023) 341650, https://doi.org/10.1016/j.aca.2023.341650.
[27] N. Al-Janabi, P. Hill, L. Torrente-Murciano, A. Garforth, P. Gorgojo, F. Siperstein, X. Fan, Mapping the Cu-BTC metal–organic framework (HKUST-1) stability envelope in the presence of water vapour for CO_2 adsorption from flue gases, Chem. Eng. J. 281 (2015) 669–677, https://doi.org/10.1016/j.cej.2015.07.020.
[28] A.M. Varghese, K.S.K. Reddy, G.N. Karanikolos, An in-situ-grown Cu-BTC metal–organic framework / graphene oxide hybrid adsorbent for selective hydrogen storage at ambient temperature, Ind. Eng. Chem. Res. 61 (2022) 6200–6213, https://doi.org/10.1021/acs.iecr.1c04710.
[29] S. Elmehrath, H.F. El-Maghraby, Y.E. Greish, Enhancing the stability of Cu-BTC metal-organic framework via the formation of cu-BTC@$Cu_3(PO_4)_2$ MOF core-shell nanoflower hierarchical hybrid composites, Adv. Mater. Interfaces 10 (2023) 2300075, https://doi.org/10.1002/admi.202300075.
[30] T. Haldar, J.W. Shiu, R.X. Yang, W.Q. Wang, H.T. Wu, H.I. Mao, C.W. Chen, C. H. Yu, Exploring MOF-derived CuO/rGO heterostructures for highly efficient room temperature CO2 sensors, ACS Sens. 9 (2024) 5856–5865, https://doi.org/10.1021/acssensors.4c01397.
[31] R. Sakthivel, L.Y. Lin, Y.F. Duann, H.H. Chen, C. Su, X. Liu, J.H. He, R.J. Chung, MOF-derived cu-BTC nanowire-embedded 2D leaf-like structured ZIF composite-based aptamer sensors for real-time in vivo insulin monitoring, ACS Appl. Mater. Interfaces 14 (2022) 28639–28650, https://doi.org/10.1021/acsami.2c06785.
[32] A.S. Duke, E.A. Dolgopolova, R.P. Galhenage, S.C. Ammal, A. Heyden, M.D. Smith, D.A. Chen, N.B. Shustova, Active sites in copper-based metal–organic frameworks: understanding substrate dynamics, redox processes, and valence-band structure, J. Phys. Chem. C 119 (2015) 27457–27466, https://doi.org/10.1021/acs.jpcc.5b08053.
[33] P.A. Koyale, S.P. Kulkarni, J.L. Gunjakar, T.D. Dongale, S.S. Sutar, S.S. Soni, Y. G. Kapdi, R. Nath R, S.V. Mulik, S.D. Delekar, ZnO nanorod/multiwalled carbon nanotube composites sensitized with Cu-based metal–organic frameworks as photoanodes for solar-driven water splitting, ACS Appl. Nano Mater. 7 (2024) 2662–2674, https://doi.org/10.1021/acsanm.3c04694.
[34] P. Koley, S.C. Shit, T. Yoshida, H. Ariga-Miwa, T. Uruga, T. Hosseinnejad, S. Periasamy, S.-I. In, D.D. Mandaliya, R.D. Gudi, Y. Iwasawa, S.K. Bhargava, Elucidation of active sites and mechanistic pathways of a heteropolyacid/cu-metal–organic framework catalyst for selective oxidation of 5-hydroxymethylfurfural via ex situ X-ray absorption spectroscopy and in situ attenuated total reflection-infrared studies, ACS Catal. 13 (2023) 6076–6092, https://doi.org/10.1021/acscatal.3c00872.
[35] T. Haldar, J.W. Shiu, R.X. Yang, W.Q. Wang, H.T. Wu, H.I. Mao, C.W. Chen, C. H. Yu, Exploring MOF-derived CuO/rGO heterostructures for highly efficient room temperature CO_2 sensors, ACS Sens. 9 (2024) 5856–5865, https://doi.org/10.1021/acssensors.4c01397.
[36] S.K. Lee, J.W. Yang, H.H. Kim, S.B. Jo, B. Kang, H. Bong, H.C. Lee, G. Lee, K.S. Kim, K. Cho, Inverse transfer method using polymers with various functional groups for controllable graphene doping, ACS Nano 8 (2014) 7968–7975, https://doi.org/10.1021/nn503329s.
[37] H.L.K.S. Mosch, O. Akintola, W. Plass, S. Höppener, U.S. Schubert, A. Ignaszak, Specific surface versus electrochemically active area of the carbon/polypyrrole capacitor: correlation of ion dynamics studied by an electrochemical quartz crystal microbalance with BET surface, Langmuir 32 (2016) 4440–4449, https://doi.org/10.1021/acs.langmuir.6b00523.
[38] Y. Yoon, B. Yan, Y. Surendranath, Suppressing ion transfer enables versatile measurements of electrochemical surface area for intrinsic activity comparisons, J. Am. Chem. Soc. 140 (2018) 2397–2400, https://doi.org/10.1021/jacs.7b10966.
[39] A. Karmakar, S. Kundu, A concise perspective on the effect of interpreting the double layer capacitance data over the intrinsic evaluation parameters in oxygen evolution reaction, Mater. Today Energ. 33 (2023) 101259, https://doi.org/10.1016/j.mtener.2023.101259.
[40] R.S. Nicholson, I. Shain, Theory of stationary electrode polarography for a chemical reaction coupled between two charge transfers, Anal. Chem. 37 (1965) 178–190, https://doi.org/10.1021/ac60221a002.
[41] F. Garay, H.E.R. Lucas, K. Malaie, Cyclic voltammetry of ion-coupled electron transfer reactions in permeable redox films: the MnO_2 case, J. Phys. Chem. C 129 (2025) 11813–11821, https://doi.org/10.1021/acs.jpcc.5c01468.
[42] H. Chahiyan, F. Gharib, A. Farajtabar, Thermodynamic studies on solubility and protonation constant of acetaminophen at different ionic strengths and various temperatures, J. Mol. Liq. 199 (2014) 137–142, https://doi.org/10.1016/j.molliq.2014.08.033.
[43] B. Hernández, F. Pflüger, S.G. Kruglik, R. Cohen, M. Ghomi, Protonation–deprotonation and structural dynamics of antidiabetic drug metformin, J. Pharm. Biomed. Anal. 114 (2015) 42–48, https://doi.org/10.1016/j.jpba.2015.04.041.
[44] B. Rezaei, S. Damiri, Electrochemistry and adsorptive stripping voltammetric determination of amoxicillin on a multiwalled carbon nanotubes modified glassy carbon electrode, Electroanalysis 21 (2009) 1577–1586, https://doi.org/10.1002/elan.200804571.
[45] H.J. Park, J.H. Yoon, K.G. Lee, B.G. Choi, Potentiometric performance of flexible pH sensor based on polyaniline nanofiber arrays, Nano Conv. 6 (2019) 9, https://doi.org/10.1186/s40580-019-0179-0.
[46] H. Shayani-Jama, D. Nematollahi, Electrochemical evidences in oxidation of acetaminophen in the presence of glutathione and N-acetylcysteine, Chem. Commun. 46 (2010) 409–411, https://doi.org/10.1039/B916458H.
[47] R. Mirzajani, S. Karimi, Preparation of γ-Fe_2O_3/hydroxyapatite/Cu(II) magnetic nanocomposite and its application for electrochemical detection of metformin in urine and pharmaceutical samples, Sens Actuators B Chem. 270 (2018) 405–416, https://doi.org/10.1016/j.snb.2018.05.032.
[48] N. AlMasoud, T.S. Alomar, Y. Xu, C. Lima, R. Goodacre, Rapid detection and quantification of paracetamol and its major metabolites using surface enhanced Raman scattering, Analyst 148 (2023) 1805–1814, https://doi.org/10.1039/D3AN00249G.
[49] K.I. Hadjiivanov, D.A. Panayotov, M.Y. Mihaylov, E.Z. Ivanova, K.K. Chakarova, S. M. Andonova, N.L. Drenchev, Power of infrared and Raman spectroscopies to characterize metal-organic frameworks and investigate their interaction with guest molecules, Chem. Rev. 121 (2021) 1286–1424, https://doi.org/10.1021/acs.chemrev.0c00487.
[50] L.Y. Pfund, C.P. PriceJessica, J. Frick, A.J. Matzger, Controlling pharmaceutical crystallization with designed polymeric heteronuclei, J. Am. Chem. Soc. 137 (2015) 871–875, https://doi.org/10.1021/ja511106j.
[51] R.C. Castro, D.S.M. Ribeiro, J.L.M. Santos, C. Nunes, S. Reis, R.N.M.J. Páscoa, Chemometric-assisted surface-enhanced Raman spectroscopy for metformin determination using gold nanoparticles as substrate, Spectrochim. Acta A: Mol. Biomol. Spectrosc. 287 (2023) 122118, https://doi.org/10.1016/j.saa.2022.122118.
[52] Y. Deng, A.D. Handoko, Y. Du, S. Xi, B.S. Yeo, In situ Raman spectroscopy of copper and copper oxide surfaces during electrochemical oxygen evolution reaction: identification of CuIII oxides as catalytically active species, ACS Catal. 6 (2016) 2473–2481, https://doi.org/10.1021/acscatal.6b00205.
[53] J.M. Park, C.M. Kim, S.H. Jhung, Melamine/polyaniline-derived carbons with record-high adsorption capacities for effective removal of phenolic compounds from water, Chem. Eng. J. 420 (2021) 127627, https://doi.org/10.1016/j.cej.2020.127627.
[54] D.T. Nguyen, H.N. Tran, R.S. Juang, N.D. Dat, F. Tomul, A. Ivanets, S.H. Woo, A. Hosseini-Bandegharaei, V.P. Nguyen, H.P. Chao, Adsorption process and mechanism of acetaminophen onto commercial activated carbon, J. Environ. Chem. Eng. 8 (2020) 104408, https://doi.org/10.1016/j.jece.2020.104408.
[55] E.P. Randviir, A cross examination of electron transfer rate constants for carbon screen-printed electrodes using electrochemical impedance spectroscopy and cyclic voltammetry, Electrochim. Acta 286 (2018) 179–186, https://doi.org/10.1016/j.electacta.2018.08.021.
[56] V. Sanko, A. Şenocak, S.O. Tümay, Y. Orooji, E. Demirbas, A. Khataee, An electrochemical sensor for detection of trace-level endocrine disruptor bisphenol A

using $Mo_2Ti_2AlC_3$ MAX phase/MWCNT composite modified electrode, Environ. Res. 212 (2022) 113071, https://doi.org/10.1016/j.envres.2022.113071.
[57] F. Marken, A. Neudeck, A.M. Bond, Cyclic voltammetry, in: F. Scholz (Ed.), Electroanalytical Methods, Springer, Berlin, Heidelberg, 2005, https://doi.org/10.1007/978-3-662-04757-6_4.
[58] J. González, E. Laborda, Á. Molina, Voltammetric kinetic studies of electrode reactions: guidelines for detailed understanding of their fundamentals, J. Chem. Educ. 100 (2023) 697–706, https://doi.org/10.1021/acs.jchemed.2c00944.
[59] M.G. Trachioti, A.C. Lazanas, M.I. Prodromidis, Shedding light on the calculation of electrode electroactive area and heterogeneous electron transfer rate constants at graphite screen-printed electrodes, Microchim. Acta 190 (2023) 251, https://doi.org/10.1007/s00604-023-05832-w.
[60] B. Wang, V. Likodimos, A.J. Fielding, R.A.W. Dryfe, In situ Electron paramagnetic resonance spectroelectrochemical study of graphene-based supercapacitors: comparison between chemically reduced graphene oxide and nitrogen-doped reduced graphene oxide, Carbon 160 (2020) 236–246, https://doi.org/10.1016/j.carbon.2019.12.045.
[61] X. Liang, Y. Zhou, J.M.S. Almeida, C.M.A. Brett, A novel electrochemical acetaminophen sensor based on multiwalled carbon nanotube and poly(neutral red) modified electrodes with electropolymerization in ternary deep eutectic solvents, J. Electroanal. Chem. 936 (2023) 117366, https://doi.org/10.1016/j.jelechem.2023.117366.
[62] W. Si, W. Lei, Z. Han, Y. Zhang, Q. Hao, M. Xia, Electrochemical sensing of acetaminophen based on poly(3,4-ethylenedioxythiophene)/graphene oxide composites, Sens. Actuators B 193 (2014) 823–829, https://doi.org/10.1016/j.snb.2013.12.052.
[63] L. Magerusan, F. Pogacean, S. Pruneanu, Enhanced acetaminophen electrochemical sensing based on nitrogen-doped graphene, Int. J. Mol. Sci. 23 (2022) 14866, https://doi.org/10.3390/ijms232314866.
[64] K. Theyagarajan, B.A. Lakshmi, Y.J. Kim, Electrochemical sensing of acetaminophen in biofluids, pharmaceutical and environmental samples using cobalt hexacyanoferrate decorated iron terephthalate metal organic framework, Electrochim. Acta 488 (2024) 144229, https://doi.org/10.1016/j.electacta.2024.144229.
[65] J.N. Baby, B. Akila, T.W. Chiu, S. Sakthinathan, A. Sherlin V, A. Zealma B, M. George, Deep eutectic solvent-assisted synthesis of a strontium tungstate bifunctional catalyst: investigation on the electrocatalytic determination and photocatalytic degradation of acetaminophen and metformin drugs, Inorg. Chem. 62 (2023) 8249–8260, https://doi.org/10.1021/acs.inorgchem.3c00676.
[66] A. Arenas-Hernandez, F.E. Cancino-Gordillo, U. Pal, $Ni_{1-x}Mn_xCo_2O_4$ nanoparticles as high-performance electrochemical sensor materials for acetaminophen monitoring, ACS Omega 10 (2025) 11250–11263, https://doi.org/10.1021/acsomega.4c10927.
[67] N.F.B. Azeredo, J.M. Gonçalves, I.S. Lima, K. Araki, J. Wang, L. Angnes, Screen-printed nickel-cerium hydroxide sensor for acetaminophen determination in body fluids, ChemElectroChem 8 (2021) 2505–2511, https://doi.org/10.1002/celc.202100417.
[68] F. Hasanpour, M. Taei, S. Tahmasebi, Ultra-sensitive electrochemical sensing of acetaminophen and codeine in biological fluids using $CuO/CuFe_2O_4$ nanoparticles as a novel electrocatalyst, J. Food Drug Anal. 26 (2018) 879–886, https://doi.org/10.1016/j.jfda.2017.10.001.
[69] L. Qian, R. Elmahdy, A.R. Thiruppathi, A. Chen, An ultrasensitive electrochemical sensor for the detection of acetaminophen via a three-dimensional hierarchical nanoporous gold wire electrode, Analyst 146 (2021) 4525–4534, https://doi.org/10.1039/D1AN00755F.
[70] J. Wang, S. Liu, J. Luo, S. Hou, H. Song, Y. Niu, C. Zhang, Conductive metal-organic frameworks for amperometric sensing of paracetamol, Front. Chem. 8 (2020) 594093, https://doi.org/10.3389/fchem.2020.594093.
[71] S. Menon, S. Jesny, K.G. Kumar, A voltammetric sensor for acetaminophen based on electropolymerizedmolecularly imprinted poly(o-aminophenol) modified gold electrode, Talanta 179 (2018) 668–675, https://doi.org/10.1016/j.talanta.2017.11.074.
[72] V. Duraisamy, V. Sudha, V. Dharuman, S.M.S. Kumar, Highly efficient electrochemical sensing of acetaminophen by cobalt oxide-embedded nitrogen-doped hollow carbon spheres, ACS Biomater Sci. Eng. 9 (2023) 1682–1693, https://doi.org/10.1021/acsbiomaterials.2c01248.
[73] S. Murugan, G. Srinivasan, W. Jeyaraj, K. Thangavel, G.E. Eldesoky, M. Govindasamy, Non-enzymatic electrochemical sensor for acetaminophen determination based on ternary composite (Fe_2O_3 @ rGO/CNF) hybrid modified electrode, J. Electrochem. Soc. 172 (2025) 037507, https://doi.org/10.1149/1945-7111/adb90d.
[74] Y. Hao, H. Zhang, X. Yue, Z. Zhao, S. Zhao, A novel electrochemical sensor based on cu(II) metal organic framework for the determination of metformin, Microchem. J. 191 (2023) 108849, https://doi.org/10.1016/j.microc.2023.108849.
[75] L. Wu, X. Lu, Y. Wu, C. Huang, C. Gua, Y. Tian, J. Ma, An electrochemical sensor based on synergistic enhancement effects between nitrogen-doped carbon nanotubes and copper ions for ultrasensitive determination of anti-diabetic metformin, Sci. Total Environ. 878 (2023) 163120, https://doi.org/10.1016/j.scitotenv.2023.163120.
[76] A. Górska, B. Paczosa-Bator, J. Wyrwa, R. Piech, New electrochemical sensor of prolonged application for metformin determination based on hydrated ruthenium dioxide-carbon black-nafion modified glassy carbon electrode, Electroanalysis 32 (2020) 1875–1884, https://doi.org/10.1002/elan.202060012.